

Microscopic Origin of Polarization-Controlled Magnetization Switching in FePt/BaTiO₃

Qurat ul ain^{1,2}*, Thi H. Ho³, Soon Cheol Hong², Dorj Odkhuu⁴, and S. H. Rhim^{2†}

¹ Department of Physics, Quaid-i-Azam University,

Islamabad, 45320, Pakistan

²Department of Physics and Energy Harvest-Storage Research Center,

University of Ulsan, Ulsan, Republic of Korea

³Laboratory for Computational Physics,

Institute for Computational Science and Artificial Intelligence,

Van Lang University, Ho Chi Minh City, Vietnam

⁴Department of Physics, Incheon National University,

Incheon, Republic of Korea

(Dated: February 5, 2026)

Electric-field driven magnetization switching in FePt/BaTiO₃ (001) is demonstrated through first-principles calculations. The magnetic easy axis of FePt layer undergoes a transition from in-plane to perpendicular direction upon ferroelectric polarization reversal, a process sensitively controlled by epitaxial strain with threshold strain strain(η) $\eta \approx \%$. At this phenomena, a large interfacial magnetoelectric coupling ($\alpha_I = 3.6 \times 10^{-10}$ G·cm²/V) is responsible, stemming from the orbital reconstruction. In particular, the redistribution of Pt-*d* orbital occupancy alters spin-orbit coupling, thereby tuning the competition between magnetic anisotropy (K_i) and magnetoelastic energy (b_1). Our work clarifies the fundamental physics of strain-engineered magnetoelectricity and suggests a concrete pathway for designing ultra-low-power voltage-controlled magnetic memory.

Introduction

The quest for "Beyond CMOS technology" has intensified the search for voltage-controlled magnetism and energy-efficient material platforms for next-generation information processing[1–3]. Among these concepts, the magnetoelectric spin-orbit (MESO) device[4] combines magnetoelectric (ME) switching for electric-field control with spin-orbit-based readout that exploits inverse Rashba-Edelstein and inverse spin Hall effects[5–7]. To realize such low-power operation, a robust coupling between electric polarization and magnetization is essential, particularly within thin-film architectures compatible with device integration.

Composite multiferroic heterostructures, comprising ferroelectric (FE) and ferromagnetic (FM) stacks, provide a practical platform for electric-field control of magnetism[8, 9]. Among various magnetoelectric (ME) coupling channels, the strain-mediated route is notably robust and scalable[10–12]. In this approach, electric-field-induced strain in the FE layer is transmitted across the interface to the FM, modulating its magnetic anisotropy through magnetoelasticity[13–15]. This mechanism is most effective when an FE layer with a large piezoelectric response is coupled to an FM with strong magnetostriction.

FePt/BaTiO₃ (BTO) is an attractive platform in this regard: ferroelectric BTO exhibits large piezoelectricity[16, 17], while FePt possesses large saturation magnetization, strong magnetocrystalline anisotropy, and appreciable magnetostriction[18–20]. While voltage-controlled magnetization reorientation has been already demonstrated[21, 22], the underlying microscopic mechanism deserves investigation. In particular, the competition between magnetic anisotropy (K_i) and magnetoelastic energy (b_1) has not been established.

In this work, first-principles electronic-structure calculations are employed to uncover strain-driven polarization control of magnetization in FePt/BaTiO₃(001). We predict a sizable interfacial magnetoelectric coefficient, $\alpha_I = 3.6 \times 10^{-10}$ G·cm²/V, originating from polarization-induced orbital reconstruction at the interface. Crucially, polarization reversal, coupled with epitaxial strain, switches the FePt easy axis between perpendicular and in-plane. This switching, governed by the interplay between interfacial uniaxial anisotropy (K_2^i) and the first-order magnetoelastic coefficient (b_1), reveals the microscopic origin of voltage-controlled magnetization switching in FePt/BTO. These results provide fundamental design guidance for low-power spintronic devices based on strain-engineered interfaces.

Computational methods

Density functional theory (DFT) calculations are performed using the the Vienna *ab initio* simulation package (VASP) [23] with the plane-wave projector augmented wave (PAW) basis [24]. The exchange-correlation potential is treated using the generalized gradient approximation (GGA) of Perdew, Burke, and Ernzerhof [25]. Energy cutoff of 450 eV is used, with Gaussian smearing $\sigma = 0.05$ eV, and k -point mesh of $15 \times 15 \times 1$ is employed for structural relaxation.

The FePt/BaTiO₃ heterostructure is modeled using 6 monolayers (ML) of FePt(001) on 12 ML (equivalent to 5.5 unit cells) of BaTiO₃ (001) with a 15 Å vacuum region. As illustrated in Fig. 1, the interface (I) region consists of single Fe, Pt, TiO₂, and BaO layers. Fe atoms occupy top site on the O atom of TiO₂ layer. All layers are allowed to relax except for four bottom-most BTO unit cells, which are fixed with their bulk polarization. The net polarization along the z -axis is de-

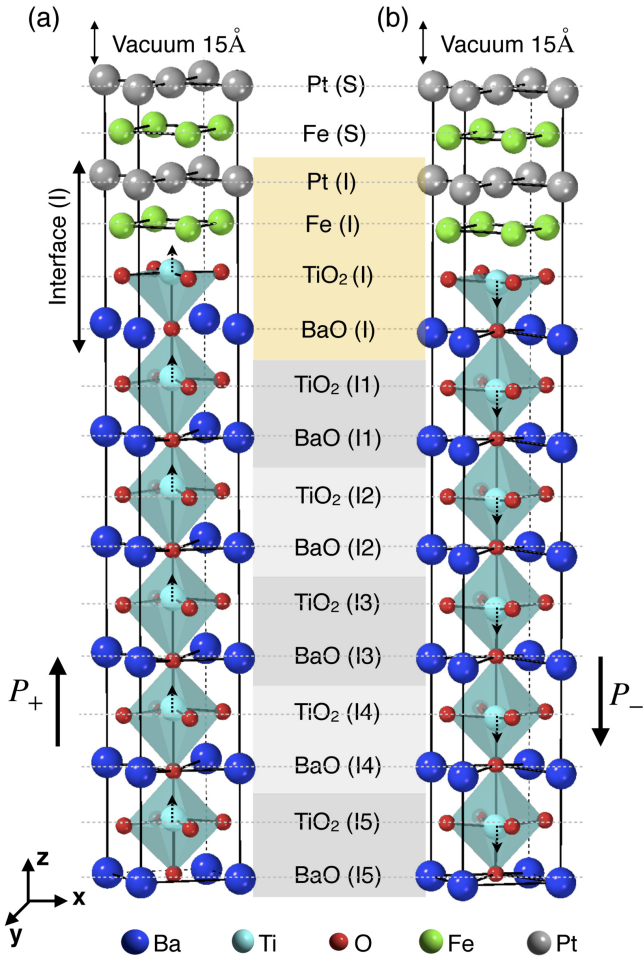


FIG. 1. Schematics of the FePt/BaTiO₃(001) heterostructure: (a) P_+ and (b) P_- , as indicated by black solid arrows. The shaded central panel highlights the regions of the surface (S), interface (I), and BaTiO₃ layer. Grey, green, blue, cyan, and red spheres represent Pt, Fe, Ba, Ti, and O atoms, respectively. Dotted arrows within the octahedra indicate the local displacements of atoms.

defined as P_+ for $z > 0$ and P_- for $z < 0$, as indicated by the solid black arrow in Fig. 1.

Optimized in-plane lattice constants of 3.99 Å for bulk BaTiO₃ and 3.87 Å for FePt are used, which agree well with experiment[26, 27]. Accordingly, 3% lattice mismatch is observed for in-plane FePt with a lattice constant of 3.87 Å. To investigate the effect of external strain on the magnetic properties, strain (η) is varied from -2% to 3%, defined as: $\eta = (a - a_o)/a_o$, where a_o is the equilibrium lattice constant of bulk BaTiO₃. Interlayer distances are relaxed for each strain with a force convergence criterion of 1×10^{-3} eV/Å.

Spin-orbit coupling (SOC) is included in the second-variational method [28]. The magnetic anisotropy energy (E_{MA}) is estimated by $E_{MA} = [E_{100} - E_{001}]/A$, where E_{100} and E_{001} are the total energies with magnetization along the [100] and [001] directions, respectively [28]; A is the surface area. The magnetic anisotropy energy E_{MA} includes contributions from magnetoelastic and uniaxial anisotropies. For reliable

values of E_{MA} , a denser k -point mesh of $33 \times 33 \times 1$ is used.

Results and Discussion

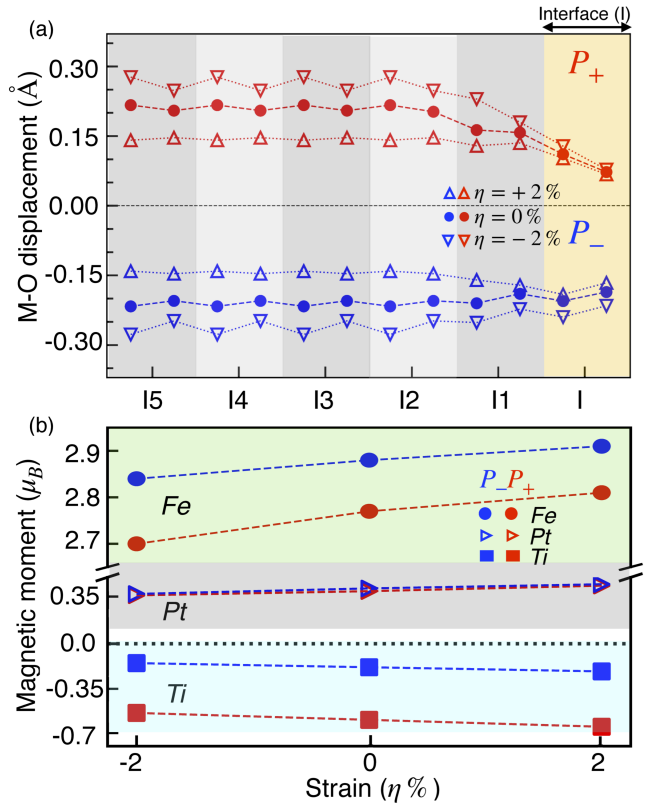


FIG. 2. (a) Relative displacement of cations (M = Ba and Ti) with respect to O plane. Filled circles and upper(lower) triangles are for 0% and ±2(-2)% strains. Shaded region corresponds to the interface (I) and BaTiO₃ regions. (b) Magnetic moment (μ_B) of interface Fe, Pt, and Ti atoms as a function of strain. Broken y-axis is separate Fe from Pt and Ti with colored shades. Circle, triangle, and square represent Fe, Pt, and Ti atoms, respectively. Red and blue denote P_+ and P_- , respectively.

The relative displacements of cations (M = Ba and Ti) are plotted in Fig. 2(a) with respect to neighboring oxygen (O) at each plane under 0% and ±2% strain for both polarization directions. Displacements along $z > 0$ ($z < 0$) correspond to cations moving towards (away from) the interface and are represented by red and blue symbols, respectively. At the interface, the M-O displacement reduces abruptly for P_+ compared to the bulk, while it remains almost unaffected for P_- irrespective of strain. Nonetheless, the relative displacements between cations and O atoms decrease (increase) with tensile (compressive) strain.

Magnetic moments of the interfacial Fe, Pt, and Ti atoms at different strain values are plotted in Fig. 2(b), with red and blue symbols for P_+ and P_- , respectively. At zero strain, magnetic moment of the interfacial Fe is 2.77 μ_B for P_+ and

$2.88 \mu_B$ for P_- , respectively. This difference in magnetic moment results from the structural sensitivity associated with the asymmetric interface-induced electric polarization. The Ti atom induces a magnetic moment of $-0.55 \mu_B$ for P_+ , which is significantly larger than the $-0.17 \mu_B$ for P_- . In contrast, Pt moment show little change under polarization reversal.

The interface magnetoelectricity is characterized by the coupling coefficient $\alpha_I = \mu_o \Delta \mu_s / \mathcal{E}$, which quantifies the difference in induced interfacial magnetization via electric polarization reversal. Here, μ_o is the vacuum permeability, $\Delta \mu_s$ is the difference in magnetic moment between P_+ and P_- , and \mathcal{E} is the external electric field [29–31]. We use the ferroelectric coercive field $\mathcal{E}_c = 120 \text{ kV/cm}$ from experiment [32]. The interface magnetoelectric coupling coefficient for FePt/BaTiO₃ is found to be $\alpha_I = 3.6 \times 10^{-10} \text{ G}\cdot\text{cm}^2/\text{V}$, which is much higher than the $2.1 \times 10^{-10} \text{ G}\cdot\text{cm}^2/\text{V}$ for Fe/BaTiO₃ [33] and $2.0 \times 10^{-10} \text{ G}\cdot\text{cm}^2/\text{V}$ for Co/Pb(Zr,Ti) [34].

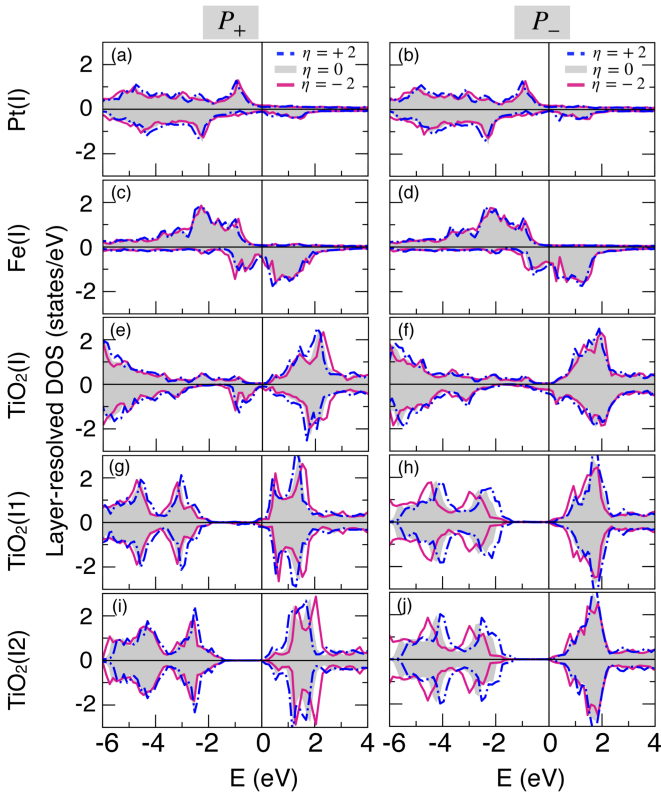


FIG. 3. Layer-resolved density of states (LDOS) for the interfacial (I) region: (a) and (b) Pt(I), (c) and (d) Fe(I), (e) and (f) TiO₂(I), and for a few inner layers: (g) and (h) TiO₂(II), (i) and (j) TiO₂(I2), for P_+ (left panels) and P_- (right panels). The filled grey region represents the LDOS at zero strain. The dashed blue and solid pink lines represent the DOS at $\pm 2\%$ strain, respectively. The vertical solid line indicates the Fermi level (E_F), which is set to zero.

To understand the interface magnetoelectric effect, layer-resolved density of states (LDOS) are plotted in Fig. 3 for P_+ (left panel) and P_- (right panel) at $\eta = 0$ and $\pm 2\%$, respectively, including LDOS of the interface layers (Pt, Fe, TiO₂)

and inner layers (TiO₂(II) and TiO₂(I2)). LDOS of BaO is not shown, as the states of BaO layers are far below the Fermi energy (E_F).

For Fe (I), the minority-spin states exhibit strong sensitivity to polarization reversal, while the majority-spin channel remains nearly unchanged, as reflected in LDOS near E_F . Specially, DOS at E_F is higher for P_- than for P_+ , indicating a polarization-dependent modulation of spin states at the interface. For TiO₂ layers away from the interface, a clear insulating behavior persists for both polarizations. In contrast, TiO₂(I) layers are distinct: for P_- , minority-spin states appear at E_F , suggesting weak spin-polarized metallicity localized at the interface. On the other hand, for P_+ , the minority-spin states of TiO₂ (I) are pushed below E_F , resulting in nearly zero DOS at E_F , consistent with the insulating nature of the BaTiO₃. Pt (I) DOS remains largely unchanged upon polarization reversal, implying that the polarization primarily alters the interfacial electronic structure within a few atomic layers. Strong hybridization occurs between the minority spin Ti- $d_{xz/yz}$ and majority spin Fe- d_{xy} states. The Ti-Fe d -orbital overlap is more significant for P_+ than for P_- , leading to a higher magnetic moment for P_+ compared to P_- . Furthermore, Pt atom induces finite magnetic moment due to Pt- $d_{x^2-y^2}$ orbital hybridization with Fe- $d_{xz/yz}$ as shown in Fig. S1 and S2 in Supplementary Material[35]. Finally, O- $2p$ orbitals lie well below E_F and show only weak overlap with Fe- $3d$ states, resulting in a small induced magnetic moment of $\sim 0.06 \mu_B$. The extent of hybridization depends on the strength of the orbital overlap, inversely on the energy separation between orbitals.

Calculated magnetic anisotropy energy (E_{MA}) is plotted in Fig. 4(a) for both polarization directions as a function of strain. E_{MA} varies linearly with strain. At $\eta = 0\%$, E_{MA} are 7.15 and 8.15 erg/cm^2 for P_+ and P_- , respectively. Notably, around $\eta = 2\%$, when the polarization changes from P_- to P_+ there is a sign change of E_{MA} , the magnetization switches from perpendicular to in-plane. This behavior is consistent with a phenomenological model [36], which treats the total magnetic energy as a sum of magnetoelastic, magnetocrystalline, and demagnetization contributions. In the model, the spin reorientation transition arises from the competition between these terms, yielding a critical strain of approximately 2% , in an excellent agreement with our present first-principles results.

Total magnetic anisotropy energy is written conveniently as

$$E_{MA} = E_{MA}^0 + b_1 t \sum_{k=1}^3 \eta_k \alpha_k^2, \quad (1)$$

where E_{MA}^0 is the magnetic anisotropy energy per area; η_k ($k = 1, 2, 3$) are the strain tensor; α_k the direction cosines of magnetization; t is the FM film thickness; b_1 is the first-order magneto-elastic (MEL) coefficient[37]; the superscript 0 denotes zero strain. In the tetragonal structure, since $\eta_1 = \eta_2$, the perpendicular strain η_3 is determined from the magneto-elastic equation of state[38]. E_{MA}^0 includes contributions of

the uniaxial anisotropy, $K_2^i(1 - \alpha_3^2)$, and the shape anisotropy, K_{sh} . In the thin film limit, the interface/surface energy dominates over the bulk counterpart. The surface contribution to shape anisotropy K_{sh} , using Bruno's relationship[39] is: $K_{sh} = -\frac{1}{2}\mu_0 M_s M_v$, where M_s is the sum of excess surface magnetization per unit area for each layer and M_v is the bulk magnetization. Strain obtained from Eq. (1) gives:

$$E_{MA} = K_{eff} + 2b_1 t \eta, \quad (2)$$

where $K_{eff} = K_2^i + K_{sh}$. As shown in Fig. 4(a), $K_2^i(1 - \alpha_3^2)$ and ME coefficient (b_1) are extracted. The uniaxial anisotropy, K_2^i , favors perpendicular magnetization ~ 7.35 and 8.44 erg/cm 2 for P_+ and P_- , respectively. The calculated shape anisotropy contribution is approximately -0.25 erg/cm 2 for both polarizations, which is small and nearly strain-independent. $K_{sh} = 0.31$ erg/cm 2 is consistent with that of 3 ML Fe/BaTiO $_3$ film[40]. Notably, the first-order magnetoelastic coefficient $b_1 = 0.18 \times 10^8$ erg/cm 3 is sufficiently large to compete with the K_2^i and thereby induce magnetization switching at $\eta = 2\%$.

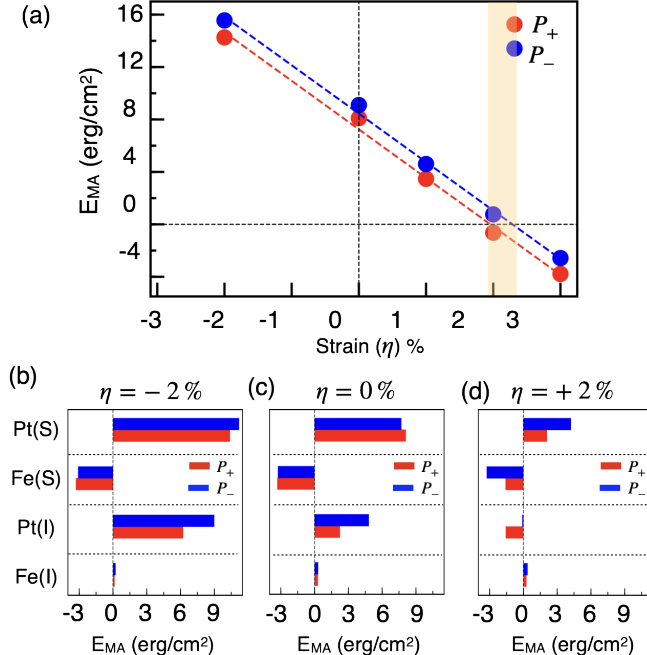


FIG. 4. Magnetic anisotropy energy (E_{MA}) of FePt/BaTiO $_3$ heterostructure as a function of strain (η). Red and blue color denote E_{MA} for P_+ and P_- , respectively. Shaded region indicates critical strain (η_c) at which magnetic anisotropy energy shifts from perpendicular to in-plane direction. Layer-resolved E_{MA} at (b) $\eta = 0\%$ and (c) $\eta = 2\%$ for polarization direction P_+ (red) and P_- (blue), respectively.

The layer-resolved atomic contributions to E_{MA} at $\eta = 0\%$ and $+2\%$ are shown in Fig. 4 (b-c), respectively. Pt atoms contribute positively to E_{MA} (> 0) at zero strain and play a dominant role in driving the magnetization switching. Under tensile strain, Pt(S) contribution decreases significantly,

while Pt(I) shifts to favor in-plane orientation. Fe atom primarily contributes to $E_{MA} (< 0)$. Under strain, Fe(S) contribution noticeably reduces in magnitude for P_+ , whereas Fe(I) contribution is negligible regardless of strain. The magnetization switching originates from the competition between uniaxial and magnetoelastic anisotropies, mainly driven by strain-induced modification of the interfacial Pt-Fe orbital hybridization and redistribution of Pt- d states near E_F as shown in Fig. 3

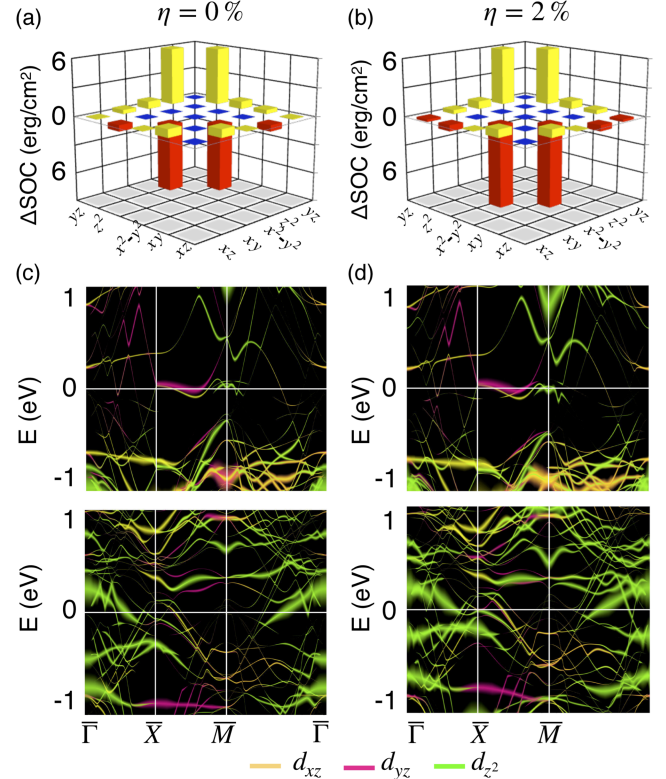


FIG. 5. Interfacial Pt d -orbital projected difference in SOC energies (ΔSOC) between in-plane and perpendicular magnetization for polarization P_+ at (a) $\eta = 0\%$ and (b) $\eta = 2\%$, where yellow, red, and blue bars represent $\Delta SOC > 0$, < 0 , and $= 0$, respectively. Orbital-resolved band structure for the majority spin (upper panel) and the minority spin (lower panel) at (c) $\eta = 0\%$ and (d) $\eta = 2\%$. Bands with yellow, magenta, and green denote xz , yz , and z^2 orbitals, respectively. The size of the symbols represents the d -orbitals.

To elucidate how strain modifies the electronic structure of the interfacial Pt atom, the difference in SOC energies (ΔSOC) are compared. ΔSOC for P_+ at 0% and 2% strain are shown in Fig. 5(a) and (b), respectively. Here, ΔSOC denotes the d -orbital-resolved difference in spin-orbit coupling energy between in-plane and perpendicular magnetization. To further understand the orbital origin of this variation, Fig. 5(c) and (d) shows the d_{xz} , d_{yz} and d_{z^2} band structure of the interfacial Pt atom along high-symmetry lines in the two-dimensional Brillouin zone for majority and minority spins. Contributions from other d -orbitals are negligible and are shown in Fig. S3

in the Supplementary Material [41]

We employ second-order perturbation theory[42] to determine E_{MA} via SOC between the occupied and unoccupied states:

$$E_{MA}^{\sigma\sigma'} = \xi^2 \sum_{o,u} \frac{|\langle o^\sigma | \hat{\ell}_z | u^{\sigma'} \rangle|^2 - |\langle o^\sigma | \hat{\ell}_x | u^{\sigma'} \rangle|^2}{E_u^{\sigma'} - E_o^\sigma}, \quad (3)$$

where ξ is the SOC constant, the radial integral of the product of the SOC amplitude $\xi(r)$; $o^\sigma(u^{\sigma'})$ and $E_o^\sigma(E_u^{\sigma'})$ are the eigenstates and eigenvalues of occupied(unoccupied) states, respectively; $\hat{\ell}_z(\hat{\ell}_x)$ is the z (x) component of the orbital angular momentum operator. This method has been successfully adopted in various *ab initio* E_{MA} explanations[38, 43–48].

Summing all features in Fig. 5(a,c) and Fig. 5(b,d), large $E_{MA} > 0$ at zero strain is attributed to $\langle yz, xz \uparrow | \hat{L}_x | z^2 \downarrow \rangle$ element along \overline{XM} . These bands remain unaffected under strain. However, at zero strain, $\langle x^2 - y^2 \downarrow | \hat{L}_x | xy \uparrow \rangle$ along $M\Gamma$ yields $E_{MA} < 0$, and its magnitude increases under strain. This enhancement in in-plane E_{MA} is evident from the shifting of unoccupied minority xy orbital towards E_F as shown in Fig. S3 in the Supplementary Material. As indicated by Eq. (3), E_{MA} increases as $(E_u^{\sigma'} - E_o^\sigma)$ decreases. All other matrix element contributions almost remain nearly unchanged under strain except for the coupling between xz and yz orbitals. At $\eta = 0\%$, $\langle yz \downarrow | \hat{L}_z | xz \downarrow \rangle$ around the \overline{X} contributes $E_{MA} > 0$. Under +2% strain, the unoccupied d_{yz} band in the minority spin channel at the \overline{X} becomes prominent, contributing $E_{MA} < 0$ through the $\langle xz \downarrow | \hat{L}_x | yz \downarrow \rangle$. We conclude that strain-induced rearrangement of the interfacial Pt-*d* orbital SOC, due to charge redistribution and orbital hybridization, is responsible for the magnetization switching.

Conclusions

In summary, we presented first-principles study of voltage-controlled magnetization in FePt/BaTiO₃ heterostructure. We show that ferroelectric polarization reversal in BaTiO₃ induces interfacial orbital reconstruction which induces a significant magnetoelectric response. Our results reveal the strain-mediated switching of magnetic anisotropy, where a competition between interfacial K_2^i and b_1 determines magnetization. This competition is governed by strain-induced modifications to spin-orbit coupling of interfacial Pt-*d* orbitals. The predicted magnetization switching with ferroelectric polarization at 2% tensile strain, coupled with the large magnetoelectric coefficient. These insights not only clarify the microscopic origin of magnetoelectric coupling in FePt/BTO but also establishes a pathway towards achieving voltage-controlled spintronics through strain-engineering.

This work was supported by National Research Foundation of Korea (NRF) grant (NRF-RS-2024-00449996 and NRF-RS-2024-00451261) and by University Research Fund (URF) of Quaid-i-Azam University, Islamabad (URF-QAU, 2022-2023). We are also grateful for supercomputing Center with

supercomputing resources (KSC-2025-CRE-0016) and computational resource of the UNIST Supercomputing center.

* Email address: quratulain@qau.edu.pk

† Email address: sonny@ulsan.ac.kr

- [1] T. N. Theis and P. M. Solomon, It's time to reinvent the transistor!, *Science* **327**, 1600 (2010).
- [2] D. E. Nikonov and I. A. Young, Benchmarking of beyond-CMOS exploratory devices for logic integrated circuits, *IEEE J. Explor. Solid-State Comput. Devices Circuits* **1**, 3 (2015).
- [3] S. Manipatruni, D. E. Nikonov, and I. A. Young, Beyond CMOS computing with spin and polarization, *Nat. Phys.* **14**, 338 (2018).
- [4] S. Manipatruni, D. E. Nikonov, C.-C. Lin, T. A. Gosavi, H. Liu, B. Prasad, Y.-L. Huang, E. Bonturim, R. Ramesh, and I. A. Young, Scalable energy-efficient magnetoelectric spin-orbit logic, *Nature* **565**, 35 (2019).
- [5] V. M. Edelstein, Spin polarization of conduction electrons induced by electric current in two-dimensional asymmetric electron systems, *Solid State Commun.* **73**, 233 (1990).
- [6] J. C. R. Sánchez, L. Vila, G. Desfonds, S. Gambarelli, J. P. Attané, J. M. De Teresa, C. Magén, and A. Fert, Spin-to-charge conversion using rashba coupling at the interface between non-magnetic materials, *Nat. Commun.* **4**, 2944 (2013).
- [7] Y. Omori, F. Auvray, T. Wakamura, Y. Niimi, A. Fert, and Y. Otani, Inverse spin hall effect in a closed loop circuit, *Appl. Phys. Lett.* **104** (2014).
- [8] W. Eerenstein, N. D. Mathur, and J. F. Scott, Multiferroic and magnetoelectric materials, *Nature* **442**, 759 (2006).
- [9] H. Zheng, J. Wang, S. E. Lofland, Z. Ma, L. Mohaddes-Ardabili, T. Zhao, L. Salamanca-Riba, S. R. Shinde, S. B. Ogale, F. Bai, D. Viehland, Y. Jia, D. G. Schlom, M. Wuttig, A. Roytburd, and R. Ramesh, Multiferroic BaTiO₃-CoFe₂O₄ nanostructures, *Science* **303**, 661 (2004).
- [10] N. Sheoran, V. Kumar, and A. Kumar, Comparative study of structural, magnetic and dielectric properties of CoFe₂O₄@BiFeO₃ and BiFeO₃@CoFe₂O₄ core-shell nanocomposites, *J. Magn. Magn. Mater.* **475**, 30 (2019).
- [11] Y. Cheng, B. Peng, Z. Hu, Z. Zhou, and M. Liu, Recent development and status of magnetoelectric materials and devices, *Phys. Lett. A* **382**, 3018 (2018).
- [12] V. Shvartsman, F. Alawneh, P. Borisov, D. Kozodaev, and D. Lupascu, Converse magnetoelectric effect in CoFe₂O₄-BaTiO₃ composites with a core-shell structure, *Smart Mater. Struct.* **20**, 075006 (2011).
- [13] J. Wang, J. Hu, H. Wang, H. Jiang, Z. Wu, J. Ma, X. Wang, Y. Lin, and C. W. Nan, Electric-field modulation of magnetic properties of Fe films directly grown on BiScO₃-PbTiO₃ ceramics, *J. Appl. Phys.* **107**, 083901 (2010).
- [14] J.-M. Hu and C. W. Nan, Electric-field-induced magnetic easy-axis reorientation in ferromagnetic/ferroelectric layered heterostructures, *Phys. Rev. B* **80**, 224416 (2009).
- [15] J.-M. Hu, T. Yang, J. Wang, H. Huang, J. Zhang, L.-Q. Chen, and C. W. Nan, Purely electric-field-driven perpendicular magnetization reversal, *Nano Lett.* **15**, 616 (2015).
- [16] J. H. Haeni, P. Irvin, W. Chang, R. Uecker, P. Reiche, Y. L. Li, S. Choudhury, W. Tian, M. E. Hawley, B. Craig, A. K. Tagantsev, X. Q. Pan, S. K. Streiffer, L. Q. Chen, S. W. Kirchoefer, J. Levy, and D. G. Schlom, Room-temperature ferroelectricity in strained SrTiO₃, *Nature* **430**, 758 (2004).

[17] K. J. Choi, M. Biegalski, Y. L. Li, A. Sharan, J. Schubert, R. Uecker, P. Reiche, Y. B. Chen, X. Q. Pan, V. Gopalan, L. Q. Chen, D. G. Schlom, and C. B. Eom, Enhancement of ferroelectricity in strained BaTiO₃ thin films, *Science* **306**, 1005 (2004).

[18] S. Okamoto, N. Kikuchi, O. Kitakami, T. Miyazaki, Y. Shimada, and K. Fukamichi, Chemical-order-disorder magnetic anisotropy and exchange stiffness constant of FePt epitaxial thin films, *Phys. Rev. B* **66**, 024413 (2002).

[19] J.-U. Thiele, L. Folks, M. F. Toney, and D. K. Weller, Perpendicular magnetic anisotropy and magnetic domain structure in sputtered epitaxial FePt (001) L1₀ films, *J. Appl. Phys.* **84**, 5686 (1998).

[20] F. E. Spada, F. T. Parker, C. L. Platt, and J. K. Howard, X-ray diffraction and mössbauer studies of structural changes and L1 ordering kinetics during annealing of polycrystalline Fe₅₁Pt thin films, *J. Appl. Phys.* **94**, 5123 (2003).

[21] Y. T. Yang, J. Li, X. L. Peng, B. Hong, X. Q. Wang, H. L. Ge, D. H. Wang, and Y. W. Du, Surface-effect enhanced magnetoelectric coupling in FePt/PMN-PT multiferroic heterostructures, *AIP Adv.* **7**, 055833 (2017).

[22] L. Leiva, J. L. A. Torres, J. E. Gomez, D. V. Rodriguez, J. Milano, and A. Butera, Electric field control of magnetism in FePt/PMN-PT heterostructures, *J. Magn. Magn. Mater.* **544**, 168619 (2022).

[23] G. Kresse and J. Furthmüller, Efficient iterative schemes for ab initio total-energy calculations using a plane-wave basis set, *Phys. Rev. B* **54**, 11169 (1996).

[24] P. E. Blöchl, Projector augmented-wave method, *Phys. Rev. B* **50**, 17953 (1994).

[25] J. P. Perdew, K. Burke, and M. Ernzerhof, Generalized gradient approximation made simple, *Phys. Rev. Lett.* **77**, 3865 (1996).

[26] R. H. Dungan, D. F. Kane, and L. R. Bickford Jr., Lattice constants and dielectric properties of Barium Titanate-Barium Stannate-Strontrium Titanate bodies, *J. Am. Ceram. Soc.* **35**, 318 (1952).

[27] A. Sakuma, First principle calculation of the magnetocrystalline anisotropy energy of FePt and CoPt ordered alloys, *J. Phys. Soc. Jpn.* **63**, 3053 (1994).

[28] D. D. Koelling and B. N. Harmon, A technique for relativistic spin-polarised calculations, *J. Phys. C* **10**, 3107 (1977).

[29] M. K. Niranjan, J. P. Velev, C.-G. Duan, S. S. Jaswal, and E. Y. Tsymbal, Magnetoelectric effect at the Fe₃O₄/BaTiO₃ (001) interface: A first-principles study, *Phys. Rev. B* **78**, 104405 (2008).

[30] K. Fujita and Y. Gohda, First-principles study of magnetoelectric coupling at Fe/Bi Fe₂O₃ (001) interfaces, *Phys. Rev. Appl.* **11**, 024006 (2019).

[31] M. K. Niranjan, C.-G. Duan, S. S. Jaswal, and E. Y. Tsymbal, Electric field effect on magnetization at the Fe/MgO (001) interface, *Appl. Phys. Lett.* **96**, 222504 (2010).

[32] G. Radaelli, D. Petti, E. Plekhanov, I. Fina, P. Torelli, B. R. Salles, M. Cantoni, C. Rinaldi, D. Gutiérrez, G. Panaccione, M. Varela, S. Picozzi, J. Fontcuberta, and R. Bertacco, Electric control of magnetism at the Fe/BaTiO₃ interface, *Nat. Commun.* **5**, 1 (2014).

[33] C.-G. Duan, S. S. Jaswal, and E. Y. Tsymbal, Predicted magnetoelectric effect in Fe/BaTiO₃ multilayers: ferroelectric control of magnetism, *Phys. Rev. Lett.* **97**, 047201 (2006).

[34] O. Vlasin, R. Jarrier, R. Arras, L. Calmels, B. Warot-Fonrose, C. Marcelot, M. Jamet, P. Ohresser, F. Scheurer, R. Hertel, G. Herranz, and S. Cherifi-Hertel, Interface magnetoelectric coupling in Co/Pb (Zr, Ti) O₃, *ACS Appl. Mater. Interfaces* **8**, 7553 (2016).

[35] See Supplemental Material at <http://link.aps.org/xxx> for spin-resolved projected density of states for both polarization direction at $\eta = -2\%$ (Fig. S1) and $\eta = +2\%$ (Fig. S2).

[36] Qurat ul ain, S. C. Hong, and S. H. Rhim, Tunability of magnetism: An interplay of magnetic anisotropy and magnetoelasticity, *J. Magn.* **26**, 162 (2021).

[37] L. D. Landau and E. M. Lifshitz, *Electrodynamics of Continuous Media* (Pergamon Oxford, 1984).

[38] Qurat ul ain, D. Odkhuu, S. H. Rhim, and S. C. Hong, Enhanced voltage-controlled magnetic anisotropy via magnetoelasticity in FePt/MgO(001), *Phys. Rev. B* **101**, 214436 (2020).

[39] P. Bruno, Magnetismus von festkörpern und grenzflächen, Lecture Notes Forschungszentrum Jülich, Jülich, Germany **4** (1993).

[40] D. Odkhuu and N. Kioussis, Strain-driven electric control of magnetization reversal at multiferroic interfaces, *Phys. Rev. B* **97**, 094404 (2018).

[41] See Supplemental Material at <http://link.aps.org/xxx> for spin-resolved band structure at $\eta = 0\%$ and $\eta = +2\%$ for positive polarization.

[42] D. S. Wang, R. Wu, and A. J. Freeman, First-principles theory of surface magnetocrystalline anisotropy and the diatomic-pair model, *Phys. Rev. B* **47**, 14932 (1993).

[43] D. Odkhuu, S. H. Rhim, N. Park, and S. C. Hong, Extremely large perpendicular magnetic anisotropy of an Fe(001) surface capped by 5d transition metal monolayers: A density functional study, *Phys. Rev. B* **88**, 184405 (2013).

[44] D. Odkhuu, S. H. Rhim, W. S. Yun, and S. C. Hong, Theory of perpendicular magnetocrystalline anisotropy Fe/MgO (001), *J. Magn. Magn. Mater.* **414**, 126 (2016).

[45] Qurat ul ain, D. D. Cuong, D. Odkhuu, S. H. Rhim, and S. C. Hong, Thickness effect on magnetocrystalline anisotropy of MnPt (001) film, *J. Magn. Magn. Mater.* **467**, 69 (2018).

[46] B. Kim, Qurat ul ain, and S. H. Rhim, Strain tunability of magnetocrystalline anisotropy in Fe₃GeTe₂ thin films, *Phys. Rev. B* **109**, 174434 (2024).

[47] T. H. Ho, D. Odkhuu, S. H. Rhim, and S. C. Hong, First-principles study on magnetocrystalline anisotropy of cobalt films: hcp vs fcc, *Curr. Appl. Phys.* **41**, 148 (2022).

[48] G. H. O. Daalderop, P. Kelly, and M. F. H. Schuurmans, Magnetic anisotropy of a free-standing co monolayer and of multilayers which contain co monolayers, *Phys. Rev. B* **50**, 9989 (1994).